Shallow long-term slow slip events along the Nankai Trough detected by the GNSS-A

By

Yusuke Yokota[1] and Tadashi Ishikawa[2]

[1] Institute of Industrial Science, University of Tokyo, 4-6-1, Komaba, Meguro-ku, Tokyo 153-8505, Japan (yyokota@iis.u-tokyo.ac.jp)

[2] Hydrographic and Oceanographic Department, Japan Coast Guard, 3-1-1, Kasumigaseki, Chiyoda-ku, Tokyo 100-8932, Japan (eisei@jodc.go.jp)

Shallow long-term slow slip events along the Nankai Trough detected by the GNSS-A

Yusuke Yokota[1] and Tadashi Ishikawa[2]
[1] Institute of Industrial Science, University of Tokyo, 4-6-1, Komaba, Meguro-ku, Tokyo 153-8505, Japan (yyokota@iis.u-tokyo.ac.jp)
[2] Hydrographic and Oceanographic Department, Japan Coast Guard, 3-1-1, Kasumigaseki, Chiyoda-ku, Tokyo 100-8932, Japan (eisei@jodc.go.jp)

Various slow earthquakes (SEQs), including tremors, very-low-frequency events (VLFs) and slow slip events (SSEs) occur along megathrust zones, which generate catastrophic earthquakes[1-7]. For comprehensive understanding of the megathrust plate boundary, it is necessary to monitor such events not only on a land area (deep plate boundary) but also on a sea area (shallow plate boundary). Many shallow SEQs have been observed along pan-Pacific subduction zones[8-11], including the Nankai Trough off southwestern Japan on which megathrust earthquakes are predicted to occur[12-13]. However, a SSE with a duration on the order of a year (long-term SSE) has not been detected in a sea area. Recently, we improved the Global Navigation Satellite System (GNSS)-Acoustic combination technique (GNSS-A), which had enabled monitoring of the seafloor absolute position, to a level that can detect a transient crustal deformation. Here, we present the first detection of long-term SSE signals from seafloor geodetic observation data and discuss timings, approximate locations and magnitudes of SSEs along the Nankai Trough inferred therefrom. The results suggest features of SSEs for the strong-coupling regions and other SEQ activities, i.e., temporal synchronization with VLF and short-term SSE activities, regional complementarity with coupling and VLF regions and recurrence in the near region. Although these are similar to features observed even in deep SSEs[4,6,14], the occurrence timing for VLF activity was different depending on each generation region. The GNSS-A monitoring network that can detect SSEs will provide new basic information to promote research on subduction geophysics and megathrust earthquake disaster prevention.

In the last two decades, many kinds of SEQs, including aseismic SSEs, have been detected using onshore high-precision seismometers and GNSS networks[1-3]. Along the Nankai Trough in western Japan, where recurring interplate megathrust earthquakes have occurred[12-13] and which has a dense seismic and geodetic monitoring network, their interrelationships were discussed and compared in detail[3-6]. Most SEQs occurred not in a strong coupling region, but rather around such a region and have features of repeatedly occurring and migrating. Different types of SEQs sequentially occurred in the neighbouring region, and temporal synchronization with other SEQs was also observed.

Observation of deep and shallow SEQ analogies and differences has multidisciplinary value with respect to physical process of the plate boundary, submarine geology and earthquake disaster research. However, shallow SEQs cannot be easily monitored due to the technological difficulty of observation. With recent advances in technology, shallow SEQs, such as tremors, VLFs and short-term SSEs with durations on the order of days, have been detected by high-precision onshore seismometers, seafloor seismometers, ocean bottom pressure gauges and submarine borehole strainmeters[7-11]. However, only long-term SSEs with durations on the order of a year have not been detected in the group of shallow SEQs. From the analogy of deep long-term SSEs, GNSS-like geodetic observation is necessary to detect the shallow long-term SSEs.

A seafloor geodetic monitoring technique called as the GNSS-A was proposed in the 1980s and has been developed in the latest two decades. The GNSS-A seafloor geodetic observation majorly constrained an interplate coupling condition[15-16] along the Nankai Trough subduction zone. Recently, we improved GNSS-A technology and upgraded observation sensitivity[17] in order to detect a transient crustal deformation with durations on the order of a year. Then, the GNSS-A monitoring can reveal the occurrence of SSEs, which cannot be observed by the onshore geodetic network, as shown in Extended Data Fig. 2. The GNSS-A methodology is described in the Method section.

We first show SSE signals detected in the GNSS-A dataset in Fig. 1. Our data is listed in Supplementary Table 1. Signal detection was carried out in the procedure shown in Extended Data Fig. 3. Coseismic and postseismic effects resulting from the 2011 Tohoku-oki earthquake were preliminarily deducted as similar to those described in ref. 15. If there was no transient event, the time series can be simply approximated by a straight line. When there is a temporal change due to SSEs in the time series, the time series can be approximated by the piece-wise line. By estimating this piece-wise line, the timing and scale of deformation can be determined. We fitted straight and piece-wise lines for the time series of each site rotating a direction every 10 degrees. Since the GNSS-A sampling rate is low, this detection is not so sensitive to the duration of the SSEs. Here, we set the deformation slope of the piece-wise line to one year, which is a typical duration of a long-term SSE[14,18-19]. The significance of fitting by the piece-wise line to the straight line is verified using the c-AIC (refs 20 and 21) based on the method of ref. 22. The c-AIC is defined as the following function:

$$\text{c-AIC} = n\ln(2\pi) + n\ln\left(\frac{RSS}{n}\right) + \frac{2nk}{n-k-1} \qquad (1)$$

where n, k and RSS are the numbers of data, a model parameter and the residual sum of squares, respectively. The maximum likelihood solution minimizes this parameter. After removing a detected deformation signal, we carried out the same process once again. When the difference (Δc-AIC) between c-AICs for the straight line and the piece-wise line is greater than -6, the process terminated because there was no clear signal. The time series of seafloor positions and Δc-AICs and signal detected periods were compared with the time series of neighbour VLF activity[7] in Figs 1a – e. Details of this process are described in the Method section. Although the Tohoku-oki earthquake effects were preliminarily deducted, the remaining effects due to model uncertainty are detected as shown in Extended Data Fig. 5. Detected deformation vectors other than the Tohoku-oki effects are judged as SSE signals and are shown in Fig. 1f. Direction of the signal at site (7) in 2014 was not from south to east and was assumed to be due to deep SSE activity[18] or error, and an SSE model was not estimated for this signal.

SSE signals at offshore sites of the Bungo and Kii deep SSEs[18-19] were detected. Off the Bungo channel, signals were detected after 2015. Off the Kii channel, signals were detected in 2009 and after 2017. In addition, SSE signals at sites around the Kumano-nada were detected in 2015 and 2017. A clear signal was not obtained for the offshore regions of the Tokai deep SSE and Shikoku Island.

We discuss timings, approximate locations and magnitude scales of SSEs by estimating rectangular fault models that can explain the detected signals at offshore sites of the Bungo and Kii channels and the Kumano-nada by the grid search method. Details of the grid search method and the results are described in the Method section and are shown in Fig. 2 and Extended Data Fig. 6, respectively. Considering durations as about one year, these undersea shallow SSE models roughly follow a SEQ scaling law whereby the event magnitude is proportional to the logarithm of the duration[4] and had no significant difference from deep SSEs[14].

In a deep region around the Bungo channel, SSEs repeatedly occurred[19,23]. The most recent SSEs occurred intermittently between 2013 and 2016. Shallow SSE signals detected after 2015 indicate that the deep SSE after 2013 spread to the offshore region. According to the grid search results, there were M_w 6.1 – 6.3 events that migrated away from the Bungo channel. The north shallow SSEs in 2015 were believed to be the first step in the spread of the deep SSE to the offshore region, and this SSE sequence ended around site (4). This is the first observation of SSE migration activity connecting deep and shallow regions that was predicted in previous studies[3]. The migration speed of the shallow SSE was approximately 50 – 100 km/year. This speed is much lower than other SEQs[8] but similar with deep long-term SSEs[14].

This SSE activity proceeded around the northeastern edge of the shallow VLF activity region from north to southeast. The VLF activity also shifted to the northeast in 2015 and converged in 2016, as shown in Fig. 2b and was thought to jump across the SSE region around sites (3) and (4). The activities of these VLFs and SSEs synchronized in time, while their activity regions were complementary.

Off the Kii channel, according to the grid search result, the M_w 6.2 SSE and the M_w 6.6 SSE were estimated in 2009 and 2017 – 2018, respectively. These SSEs repeatedly occurred at eight-year intervals. In this region, detailed shallow VLF source reanalysis was performed considering the 3D structure[24]. According to this analysis, VLFs were strongly activated in 2009 and 2018. Although there was an activity in 2015, this activity was smaller than other two cases. The VLF activity in 2009 was slightly closer to the western side than in 2018, as shown in Fig. 2b. The 2009 SSE was also located in the western part of the 2017 – 2018 SSE region, although spreading to the west cannot be sufficiently constrained because there was no western site before 2011. This consistency suggests the temporal synchronization and the spatial correlation between SSE and VLF in this region. Unlike the Bungo case, the SSE appears to precede the VLF activity.

The M_w 6.1 SSEs estimated off Kumano-nada were in the vicinity of short-term SSE activity[10], although it is possible that the western SSE was due in part to an afterslip of the M_w 5.8 earthquake on Apr. 1, 2016 that occurred below this region. Since total slip amounts of short-term SSEs had been presumed small[10], the detected long-term SSEs were believed to be independent activities synchronous with the short-term SSE activity. In this region, after the eastern long-term SSE occurred in 2015, VLF activity was monitored around the area between the eastern and western long-term SSEs and was believed to be associated with short-term SSEs[11]. In this case, long-term SSEs occurred both before and after this VLF activity.

The relationship with a strong coupling region is similar to deep SSEs. Deep SSEs have a feature to occur on the deep side adjacent to a strong coupling region and a historical slip region[18-19,25]. The detected shallow SSEs are also roughly adjacent on the shallow side. This indicates that the edge areas of strong coupling regions may have two periods that accumulate coupling and release at least a part of the coupling both by a deep SSE and a shallow SSE.

Among sites other than the eight sites, no clear SSE signal was detected. The SSE signal has not been detected even by the closest site (13) to the Tokai deep SSE region[25], although this site, which has only an approximately seven-year observation period, may not yet have adequate resolution. Regions off Shikoku Island and off Tokai deep SSE are locations where strong coupling regions[15-16] overlapped assumed and historical seismogenic zones[12-13]. The absence of SSEs during our observation period indicates the possibility that these are main slip regions of the Nankai Trough megathrust zone.

The detected shallow SSEs led new knowledge and discussion about a diverse behaviour of SEQs and provide many academic targets about such as stress loading for the coupling region and difference in geological conditions in SSEs and coupling regions, to be solved by future seafloor and onshore geophysical monitoring. It is also necessary to enhance the seafloor geodetic observation system in order to upgrade the observation density and continuity for investigating a detail relation between SSEs and megathrust earthquakes.

References

(1) Dragert, H., Wang, K. & James, T. S. A silent slip event on the deeper Cascadia subduction interface. *Science* **292**, 5521, 1525-1528, doi:10.1126/science.1060152 (2001).

(2) Ozawa, S. *et al.* Detection and Monitoring of Ongoing Aseismic Slip in the Tokai Region, Central Japan. *Science* **298**, 5595, 1009–1012, doi:10.1126/science.1076780 (2002).

(3) Hirose, H., Asano, Y., Obara, K., Kimura, T., Matsuzawa, T., Tanaka, S. & Maeda, T. Slow earthquakes linked along dip in the Nankai subduction zone. *Science* **330**, 1502, doi:10.1126/science.1197102 (2010).

(4) Ide, S., Beroza, G. C., Shelly, D. R. & Uchide, T. A scaling law for slow earthquakes. *Nature* **447**, 76–79, doi:10.1038/nature05780 (2007).

(5) Ruiz, S. *et al.* Intense foreshocks and a slow slip event preceded the 2014 Iquique M_w 8.1 earthquake. *Science* **345**, 6201, 1165-1169, doi:10.1126/science.1256074 (2014).

(6) Obara, K. & Kato, A. Connecting slow earthquakes to huge earthquakes. *Science* **353**, 6296, 253-257, doi:10.1126/science.aaf1512 (2016).

(7) Asano, Y., Obara, K. & Ito, Y. Spatiotemporal distribution of very-low frequency earthquakes in Tokachi-oki near the junction of the Kuril and Japan trenches

revealed by using array signal processing. *Earth Planet. Space* **60**, 871–875, doi:10.1186/BF03352839 (2008).

(8) Yamashita, Y. *et al.* Migrating tremor off southern Kyushu as evidence for slow slip of a shallow subduction interface. *Science* **348**, 6235, 676–679, doi:10.1126/science.aaa4242 (2015).

(9) Wallace, L. M., *et al.* Slow slip near the trench at the Hikurangi subduction zone, New Zealand. *Science* **352**, 701-704, doi:10.1126/science.aaf2349 (2016).

(10) Araki, E, *et al.* Recurring and triggered slow-slip events near the trench at the Nankai Trough subduction megathrust. *Science* **356**, 1157-1160, doi:10.1126/science.aan3120 (2017).

(11) Nakano, M., Hori, T., Araki, E., Kodaira, S. & Ide, S. Shallow very-low-frequency earthquakes accompany slow slip events in the Nankai subduction zone. *Nature Comm.* **9**, 984, doi:10.1038/s41467-018-03431-5 (2018).

(12) Ando, M. Source mechanism and tectonic significance of historical earthquakes along the Nankai Trough, Japan. *Tectonophysics* **27**, 119–140, doi:10.1016/0040-1951(75)90102-X (1975).

(13) Sagiya, T. & Thatcher, W. Coseismic slip resolution along a plate boundary megathrust: The Nankai Trough, southwest Japan. *J. Geophys. Res.* **104**, B1, 1111–1129, doi:10.1029/98JB02644 (1999).

(14) Takagi, R., Uchida, N. & Obara, K. Along-strike variation and migration of long-term slow slip events in the western Nankai subduction zone, Japan. *J. Geophys. Res.*, doi:10.1029/2018JB016738 (2019).

(15) Yokota, Y., Ishikawa, T., Watanabe, S., Tashiro, T. & Asada, A. Seafloor geodetic constraint for interplate coupling along the Nankai Trough megathrust zone. *Nature* **534**, 374-377, doi:10.1038/nature17632 (2016).

(16) Nishimura, T., Yokota, Y., Tadokoro, K. & Ochi, T. Strain partitioning and interplate coupling along the northern margin of the Philippine Sea plate, estimated from Global Navigation Satellite System and Global Positioning System-Acoustic data. *Geosphere* **14**(2), doi:10.1130/GES01529.1 (2018).

(17) Yokota, Y., Ishikawa, T. & Watanabe, S. Gradient field of undersea sound speed structure extracted from the GNSS-A oceanography. *Mar. Geophys. Res.* doi:10.1007/s11001-018-9362-7 (2018).

(18) Kobayashi, A. Objective detection of long-term slow slip events along the Nankai Trough using GNSS data (1996-2016). *Earth Planet. Space* **69**, 171, doi:10.1186/s40623-017-0755-7 (2017).

(19) Ozawa, S. Long-term slow slip events along the Nankai trough subduction zone after the 2011 Tohoku earthquake in Japan. *Earth Planet. Space* **69**, 56, doi:10.1186/s40623-017-0640-4 (2017).

(20) Akaike, H. A new look at the statistical model identification. *IEEE Trans. Auto. Control* **19**, 716-723, doi:10.1109/TAC.1974.1100705 (1974).

(21) Sugiura, N. Further analysts of the data by Akaike's information criterion and the finite corrections. *Communications in Statics – Theory and Methods* **7**(1), 13-26, doi:10.1080/03610927808827599 (1976).

(22) Nishimura, T., Matsuzawa, T. & Obara, K. Detection of short-term slow slip events along the Nankai Trough, southwest Japan, using GNSS data. *J. Geophys. Res. Solid Earth* **118**, 3112–3125, doi:10.1002/jgrb.50222 (2013).

(23) Ozawa, S., Suito, H., Imakiire, T. & Murakmi, M. Spatiotemporal evolution of aseismic interplate slip between 1996 and 1998 and between 2002 and 2004, in Bungo channel, southwest Japan. *J. Geophys. Res.* **112**, B05409, doi:10.1029/2006JB004643 (2007).

(24) Takemura, S., Matsuzawa, T., Noda, A., Tonegawa, T., Asano, Y., Kimura, T. & Shiomi, K. Structural characteristics of the Nankai Trough shallow plate boundary inferred from shallow very low-frequency earthquakes. *Geophys. Res. Lett.* doi:10.1029/2019GL082448 (2019).

(25) Ozawa, S., Tobita, M. & Yarai, H. A possible restart of an interplate slow slip adjacent to the Tokai seismic gap in Japan. *Earth Planet. Space* **68**, 54, doi:10.1186/s40623-016-0430-4 (2016).

(26) Colombo, O. L. Long range kinematic GPS, in *GPS for Geodesy, 2nd Edition*, Kleusberg, A. & Teunissen, P., Editors. Springer-Verlag (1998).

(27) Colombo, O. L., Sutter, A. W. & Evans, A. G. Evaluation of precise, kinematic GPS point positioning, *Proceedings of ION GNSS-2004*, Long Beach, California, September (2004).

(28) Iwasaki, T., Sato, H., Shinohara, M., Ishiyama, T. & Hashima, A. Fundamental structure model of island arcs and subducted plates in and around Japan. *2015 Fall Meeting, American Geophys. Union, San Francisco*, Dec. 14-18, T31B-2878 (2015).

(29) Lindquist, K. G., Engle, K., Stahlke, D. & Price, E. Global Topography and Bathymetry Grid Improves Research Efforts, *Eos Trans. AGU*, **85**(19), 186, http://onlinelibrary.wiley.com/doi/10.1029/2004EO190003/abstract (2004).

(30) Altamimi, Z., Collilieux, X., Legrand, J., Garayt, B. & Boucher, C. ITRF2005: a new release of the International Terrestrial Reference Frame based on time series of

station positions and Earth Orientation Parameters. *Geophys. J. Int.* **112**, B09401, doi:10.1029/2007JB004949 (2007).

Acknowledgements

Valuable comments from T. Nishimura improved our manuscript. We would like to thank O. L. Colombo of the NASA Goddard Space Flight Center for providing us with the kinematic GNSS software "IT" (Interferometric Translocation)[26-27] and the Geospatial Information Authority of Japan (GSI) for providing us with the high-rate GNSS data for the kinematic GNSS analysis and the daily coordinates of the sites on the GSI website. The VLF catalogue was provided by Y. Asano in National Research Institute for Earth Science and Disaster Resilience (NIED). The plate models of refs 28 and 29 were constructed from topography and bathymetry data provided by the Geospatial Information Authority of Japan (250-m digital map), Japan Oceanographic Data Center (500-m mesh bathymetry data, J-EGG500, http://www.jodc.go.jp/jodcweb/JDOSS/infoJEGG_j.html) and the Geographic Information Network of Alaska, University of Alaska. In addition, many among the staff of the Hydrographic and Oceanographic Department, Japan Coast Guard (JHOD), including the crews of the S/Vs Takuyo, Shoyo, Meiyo and Kaiyo, supported our observations and data processing. Some figures were produced using the GMT software.

Author Contributions

Y.Y. and T.I. designed the study and performed the statistical processing. Y.Y. carried out the grid search analysis. Y.Y. and T.I. developed the GNSS-A seafloor geodetic observation system and wrote this manuscript.

Author Information

Correspondence and requests for materials should be addressed to Y.Y. (yyokota@iis.u-tokyo.ac.jp) or T.I. (eisei@jodc.go.jp).

Figure legends

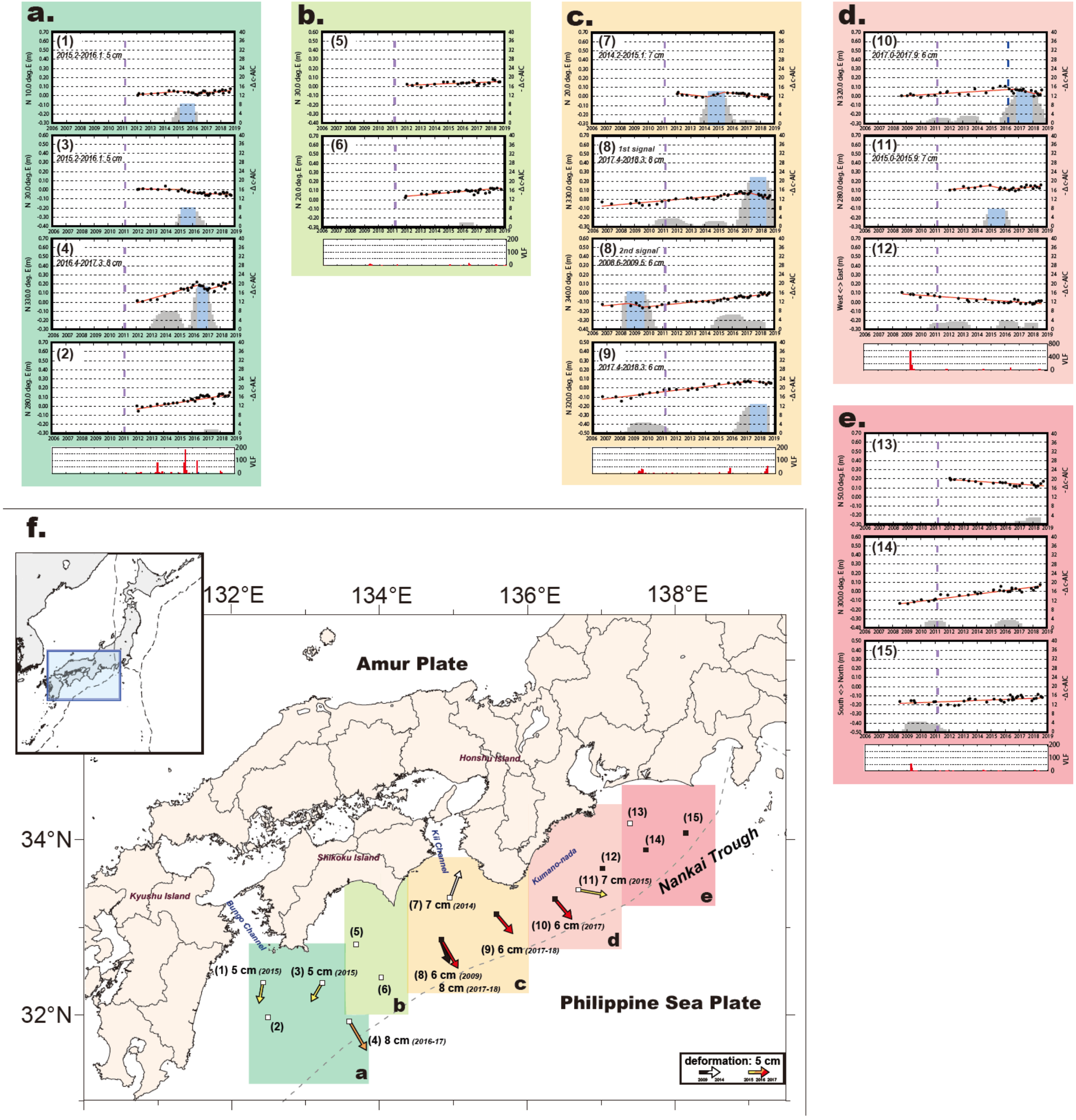

Fig. 1 | Results of the SSE signal detection process. a – e, time series of seafloor crustal deformations in the sites in coloured regions drawn in f. The maximum likelihood straight and piece-wise lines in the sites where SSE signals were detected and were not detected, respectively, were displayed. In site (8), two detected cases were displayed. Each time series was plotted in the direction for the case of the maximum likelihood solution in the SSE signal detection process. The reference frame is International Terrestrial Reference Frame (ITRF) 2005 (ref. 30). Red lines indicate straight and piece-wise lines estimated as the maximum likelihood solutions. Grey histograms are Δc-AIC time series (bin range: one year) every 0.2 years. Each light-blue bin is the case that was judged as an SSE signal. Bottom red histograms are shallow VLF numbers[7] within coloured regions in **f** every month. Purple and blue dashed lines indicate the 2011 Tohoku-oki earthquake and the 2016 M_w 5.8 earthquake in the Kumano-nada region, respectively. **f, Seafloor crustal deformations detected in the SSE signal detection process.** Vectors indicated seafloor crustal deformations detected in the GNSS-A data. Closed and open squares are the seafloor observation sites set before and after 2011, respectively.

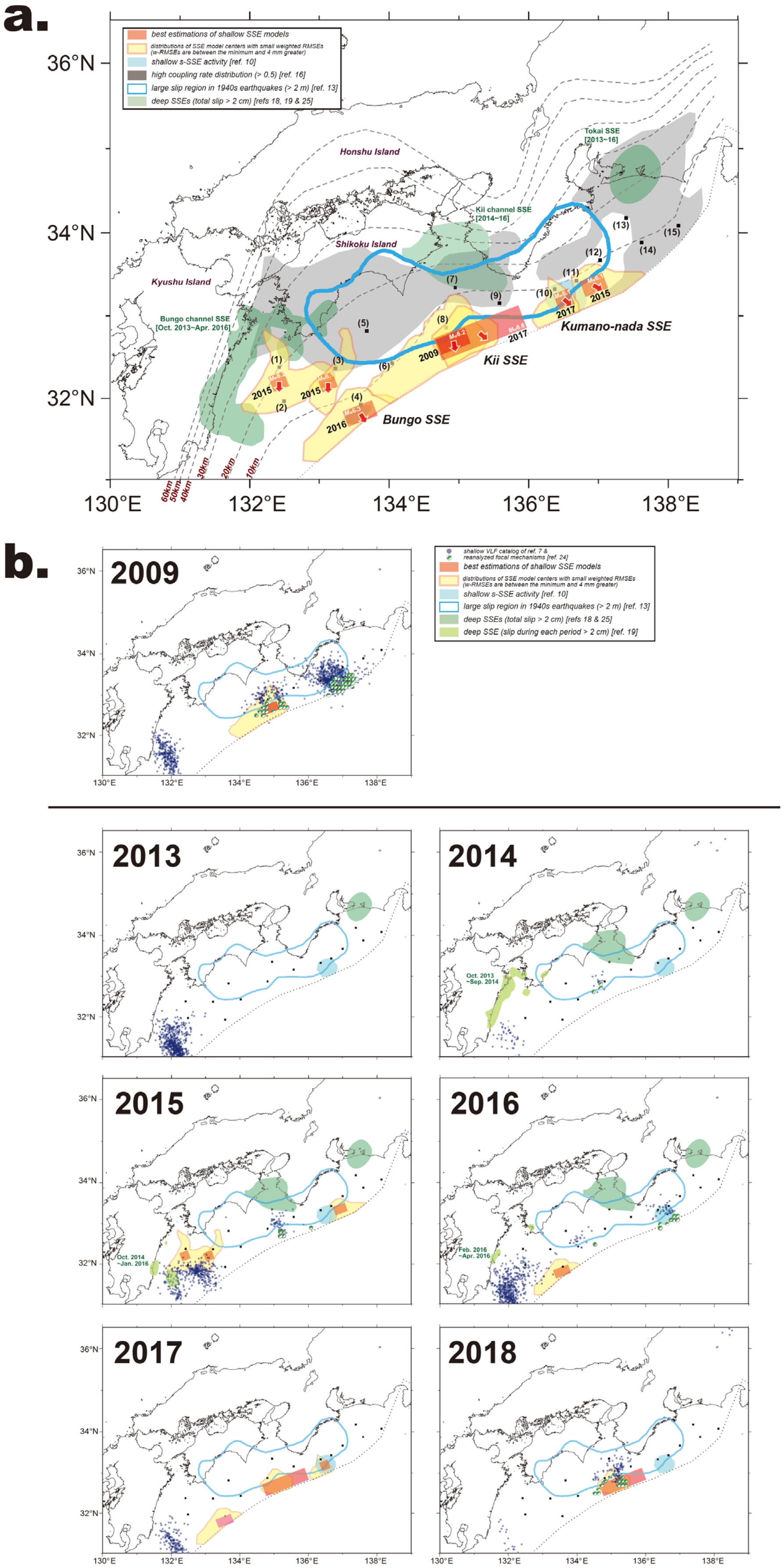

Fig. 2 | a, Spatial relationship between detected shallow SSEs, coupling rate

distribution and deep SSEs along the Nankai Trough. Red rectangles and vectors are shallow SSE models and slip angles, respectively, estimated by the grid search. The yellow regions show distributions of SSE model centres with weighted RMSEs calculated in the range between the minimum and 4 mm greater than the minimum. The light-blue polygon indicates the Kumano-nada short-term SSE activity region detected by submarine borehole monitoring[10]. The grey contour map indicates high coupling rate distribution[16] (rate: more than 0.5). The light-blue solid line indicates the most recent seismogenic region[13] (slip: more than 2 m). Green regions indicate deep SSE regions[18-19,25] (total slip: more than 2 cm). Dashed lines indicate the depths of the plate boundary of refs 28 and 29. Closed squares are the seafloor observation sites. **b, Snapshots of detected shallow SSEs in 2009 and 2012 - 2018.** Blue dots indicate shallow VLF activities[7] in each year. Green focal mechanisms of VLFs (134.5°E – 137.5°E) were estimated in ref. 24 by reanalysis of a part of the VLF catalogue of ref. 7 in consideration of the 3D structure. Green regions indicate deep Kii and Tokai SSE regions[18,25] (total slip: more than 2 cm). Light-green regions indicate deep Bungo SSE regions[19] (slip during each period: more than 2 cm).

Methods

Seafloor geodetic observation. Seafloor movements are determined combining the GNSS observation above the sea and the acoustic ranging system under the sea. This method is called the GNSS-A, which is a unique approach to monitor the absolute horizontal movement directly above the offshore interplate boundary. This technique was proposed in the 1980s (ref. 31) and established after the 1990s. We have been developing observation techniques[32-34] and have provided valuable data for geodesy and seismology, e.g., the pre-, co- and post-seismic seafloor crustal deformations of the 2011 Tohoku-oki earthquake[35-37] and the interseismic coupling condition along the Nankai Trough[15].

A schematic diagram of the seafloor geodetic observation system is shown in Extended Data Fig. 1. Before 2015, the observation frequency was approximately two to three times/year. After 2016, the acoustic system has been improved in order to observe each site four to 10 times/year (refs 38 and 39). Details of the GNSS-A system and the data were described and published in ref. 40. Dataset used in the present study was improved from published data about the underwater sound speed structure error using the method of ref. 17.

Slow slip event detectability of the GNSS-A. Detectability for SSEs was verified based on the method proposed in ref. 41. We verified whether crustal deformations calculated using the SSE fault models set on the plate boundary are observable in the onshore and seafloor geodetic monitoring networks. We assumed crustal deformations for the horizontal component in all of the sites using Green's functions calculated using the formulation of ref. 42 considering a homogeneous elastic half-space. The fault models were set depending on the magnitude of every 0.1 and were deployed every 0.1 degree on the plate boundary model (refs 28 and 29), which dip angles at shallower part than 10 km were set to roughly match seismic survey results in ref. 43. The fault size of each magnitude was set according to scaling law using in ref. 41, assuming a rigidity of 10 GPa. The strike angle of the fault model was set to 249° in most areas and was adjusted in an area where the trough axis angle was largely different. The rake angle was set to 90°.

RMSs of GNSS and GNSS-A data are about 3 mm (ref. 41) and about 2 cm or more (ref. 40), respectively. In this study, considering these observation abilities, it is judged that SSEs can be detected when the horizontal movements in the onshore and seafloor networks exceed 5 mm and 5 cm which are about twice RMSs, respectively, even at one site. Extended Data Figs 2a and b show the resultant maps calculated using the onshore network only and using the onshore and seafloor networks, respectively. Extended Data

Fig. 2c indicates SSEs which can be detected only by the seafloor network. These results show that the seafloor network can detect M_w 6 class shallow SSEs that cannot be detected using only the onshore network.

Slow slip event signal detection process using Δc-AIC. We detected an SSE signal according to the process flow shown in Extended Data Fig. 3. Before the signal detection process, the same deductions as ref. 15 on effects resulting from the 2011 Tohoku-oki earthquake were performed for the dataset. Coseismic and postseismic effects were calculated based on the models established in refs 44, 45 and 46. Resultant time series of their locations in the sites along the Nankai Trough were listed in Extended Data Fig. 4 and Supplementary Table 1. The reference frame is International Terrestrial Reference Frame (ITRF) 2005 (ref. 30).

We detected an SSE signal in these time series based on the method of ref. 22 using c-AIC (refs 20 and 21). We fitted straight and piece-wise lines for the time series and compared each c-AIC to determine if a time series contains SSE-like transient deformation. We rotated a direction of time series every 10 degrees to extract the maximum deformation angle. A deformation duration of the piece-wise line was set to one year which is a typical timescale for long-term SSE. This piece-wise line was fitted for the time series data for all periods. The residual sums of squares (RSSs) in Eq. (1) were calculated for the straight and piece-wise lines for the data for the whole periods. The start timing and scale of deformation were estimated every 0.2 years and every 1 cm between 1 and 20 cm, respectively, and were chosen to minimize c-AIC. We defined Δc-AIC as a difference between c-AICs for the straight line and the piece-wise line. When a deformation signal of Δc-AIC < -6 was detected by the piece-wise line, after removing this detected deformation, the same process was performed. When a signal of Δc-AIC < -6 was not detected, the process ended because there was no clear signal. Signals detected between 2011 and Dec. 2013 were considered to be a remaining influence due to the 2011 Tohoku-oki earthquake, even after the deduction process. We identified a signal other than this type of signal as an SSE signal.

Grid search process to determine SSE models. Each SSE fault model that explains the deformation fields determined in the c-AIC detection process was estimated using a grid search technique. We set rectangular fault models for a grid every 0.1 degree on the plate boundary to estimate the weighted RMSEs for the data in the region delimited. The strike angle was set to 249°. The fault length, width, slip and rake angles were properly changed every 10 km between 20 and 100 km, every 10 km between 20 and 50 km in the dip direction, every 4 cm between 2 and 78 cm and every 10° between 70° and 130°, respectively. The dip angle was set along the plate boundary model described in the above section "SSE detectability of the GNSS-A". Crustal deformations were also calculated using the method and setting described in the above section. We calculated crustal deformations for the horizontal component at seafloor sites and the neighbour onshore GNSS sites of the GEONET. Considering the observation abilities, the weighted RMSE was calculated by multiplying the onshore data by nine times the weight of the seafloor data.

Refs 14 and 19 showed unsteady crustal deformation fields detected by GEONET around the Bungo channel and suggested that there was no deformation fields over 5 mm in 2015 and after Apr. 2016. Crustal deformation fields[18] detected by GEONET around the Kii channel and the Kumano-nada also suggested that there was no deformation field over 5 mm in the time periods for calculating SSE models. Then, onshore crustal deformations were assumed to be less than about 5 mm in estimations. Signals off the Bungo channel in 2015 (sites (1) and (3)) and off the Kii channel in 2017 (sites (8) and (9)) were synchronized and were considered to cause each SSE sequence. However, off the Bungo channel, since it was not possible to estimate a single rectangular fault model with an onshore deformation of less than about 5 mm, a rectangular fault was estimated for each site observation. Off the Kii channel, one rectangular fault model was estimated.

Observed and calculated deformation values in the best cases are compared in Extended Data Fig. 6. The distributions of SSE model centres with weighted RMSEs calculated in the range between the minimum and 4 mm greater than the minimum are drawn in Fig. 2 and Extended Data Fig. 6. A small RMSE region can be interpreted as the fault location estimation accuracy in each case. Small RMSE regions spread in the vicinity of the trough axis, where there is no site, so it is difficult to determine not only the fault position near the trench axis but also the upper end of the magnitude.

Data availability. The dataset of seafloor positions is provided in Supplementary Table 1.

References

(31) Spiess, F. N. *et al.* Precise GPS/Acoustic positioning of seafloor reference points for tectonic studies. *Phys. Earth Planet. Inter.* **108**, 101–112 (1998).

(32) Asada, A. & Yabuki, T. Centimeter-level positioning on the seafloor. *Proc. Jpn Acad. Ser. B* **77**, 7–12 (2001).

(33) Fujita, M. *et al.* GPS/acoustic seafloor geodetic observation: method of data analysis and its application. *Earth Planet. Space* **58**, 265–275, doi:10.1007/s00190-013-0649-9 (2006).

(34) Ishikawa, T. & Yokota, Y. Detection of seafloor movement in subduction zones around Japan using a GNSS-A seafloor geodetic observation system from 2013 to 2016. *J. Disaster Res.* **13**(3), 511-517, doi:10.20965/jdr.2018.p0511 (2018).

(35) Sato, M. *et al.* Interplate coupling off northeastern Japan before the 2011 Tohoku-oki earthquake, inferred from seafloor geodetic data. *J. Geophys. Res.* **118**, 1–10, doi:10.1002/jgrb.50275 (2013).

(36) Sato, M. *et al.* Displacement above the hypocenter of the 2011 Tohoku-oki earthquake. *Science* **332**, 1395, doi:10.1126/science.1207401 (2011).

(37) Watanabe, S. *et al.* Evidence of viscoelastic deformation following the 2011 Tohoku-oki earthquake revealed from seafloor geodetic observation. *Geophys. Res. Lett.* **41**, 5789–5796, doi:10.1002/2014GL061134 (2014).

(38) Yokota, Y., Tashiro, T. & Shimomura, H. Implementation of multi-acoustic ranging system. *Rep. Hydro. Ocean Res.* **55**, 32–37 (2017).

(39) Matsushita, M. & Koike, M. Improving efficiency in seafloor geodetic observation system using a multi-acoustic ranging method. *Rep. Hydro. Ocean Res.* **56**, 46–49 (2018).

(40) Yokota, Y., Ishikawa, T. & Watanabe, S. Seafloor crustal deformation data along the subduction zones around Japan obtained by GNSS-A observations. *Scientific Data* **5**, 180182, doi:10.1038/sdata.2018.182 (2018).

(41) Suito, H. Detectability of interplate fault slip around Japan, based on GEONET daily solution F3, *Journal of Geod. Soc. Japan* **62**(3), 109-120 (2016).

(42) Okada, Y. Internal deformation due to shear and tensile faults in a half-space. *Bull. Seis. Soc. Am.* **82**(2), 1018–1040 (1992).

(43) Kimura, G., Kitamura, Y., Hashimoto, Y., Yamaguchi, A., Shibata, T., Ujiie, K. & Okamoto, S. Transition of accretionary wedge structures around the up-dip limit of the seismogenic subduction zone. *Earth Planet. Sci. Lett.* **255**, 471-484, doi:10.1016/j.epsl.2007.01.005 (2007).

(44) Iinuma, T., *et al.* Coseismic slip distribution of the 2011 off the Pacific Coast of Tohoku Earthquake (M9.0) refined by means of seafloor geodetic data. *J. Geophys. Res.* **117**, B07409, doi:10.1029/2012JB009186 (2012).

(45) Sun, T. *et al.* Prevalence of viscoelastic relaxation after the 2011 Tohoku-oki earthquake. *Nature* **514**, 84–87, doi:10.1038/nature13778 (2014).

(46) Sun, T. & Wang, K. Viscoelastic relaxation following subduction earthquakes and its effects on afterslip determination. *J. Geophys. Res.* **120**, 1329–1344, doi:10.1002/2004JB011707 (2015).

Extended Data legends

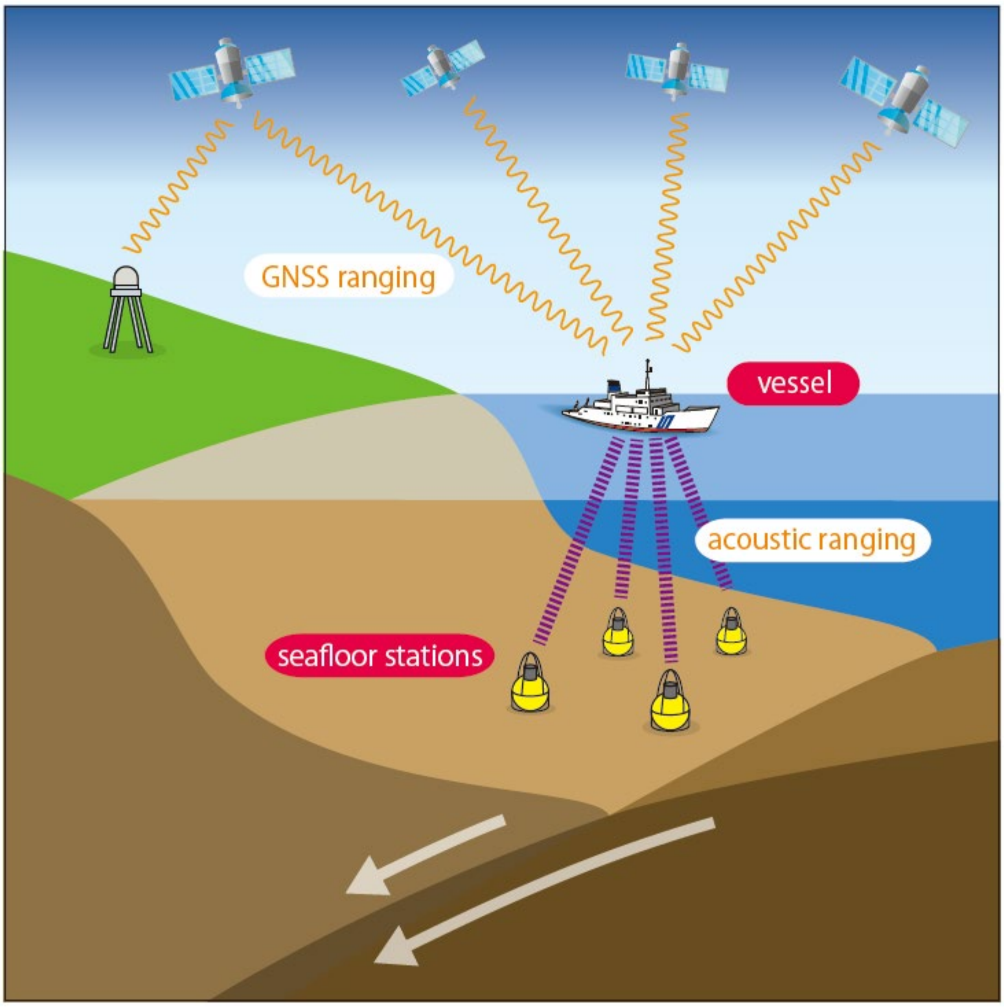

Extended Data Figure 1 | Schematic diagram of the GNSS-A seafloor geodetic observation system. This figure is modified from refs 15, 17, 32, 33 and 34.

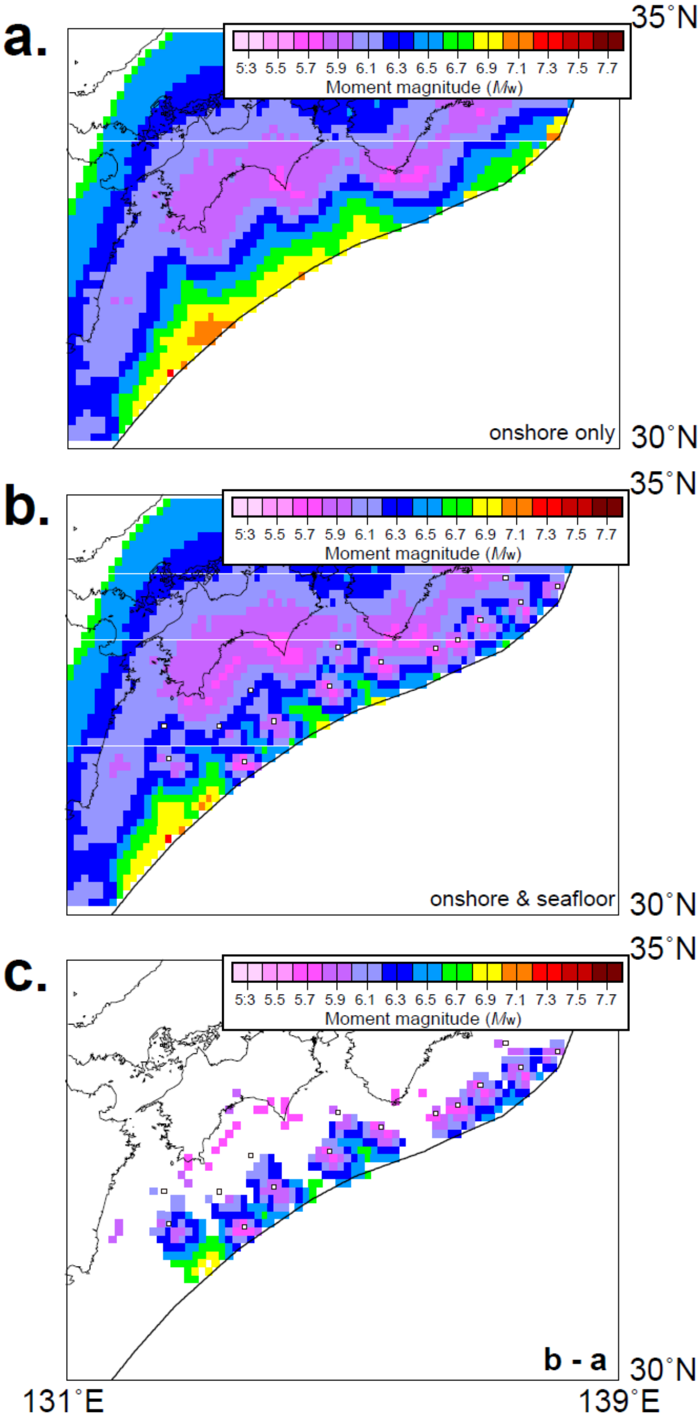

Extended Data Figure 2 | Maps representing SSE detectability constructed using, a, the onshore GNSS network only and, b, onshore and seafloor GNSS-A networks. c, Maps representing SSEs which can be detected only by the seafloor GNSS-A network. Colour contours indicate the magnitude of detectable minimum events at each grid on the plate boundary.

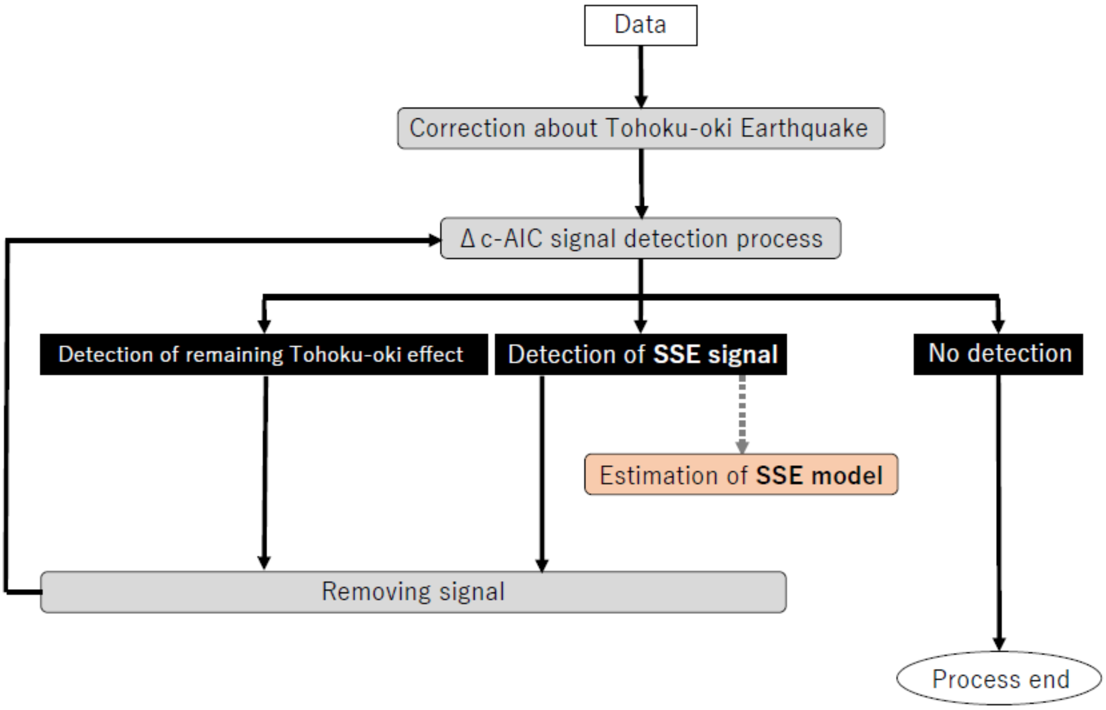

Extended Data Figure 3 | Flow of the SSE signal detection process.

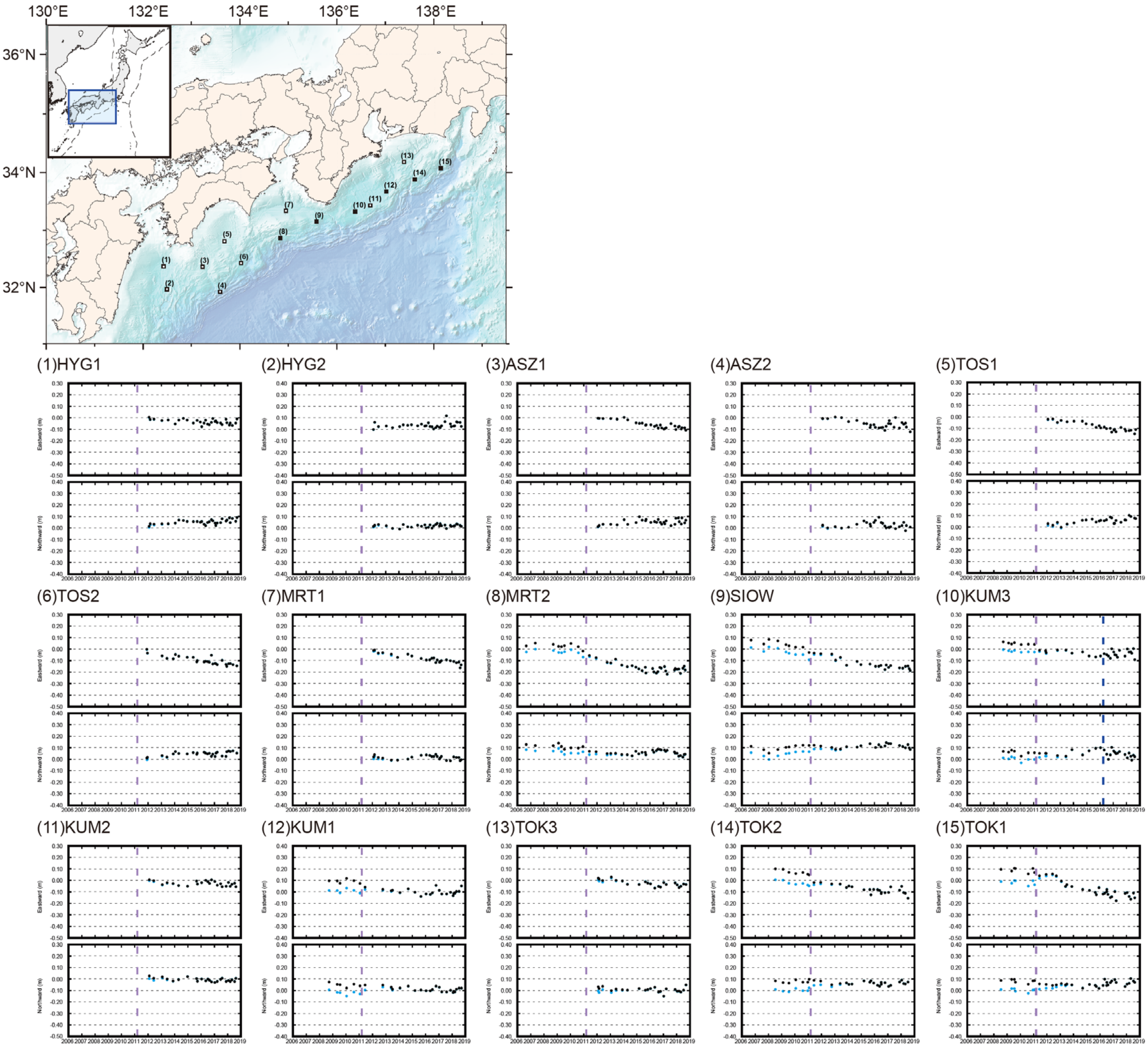

Extended Data Figure 4 | Time series of horizontal components of seafloor GNSS-A data. Black circles indicate seafloor positions after deduction of deformations due to the 2011 Tohoku-oki earthquake based on refs 44, 45 and 46. Blue circles indicate raw data before deduction. The reference frame is ITRF2005 (ref. 30).

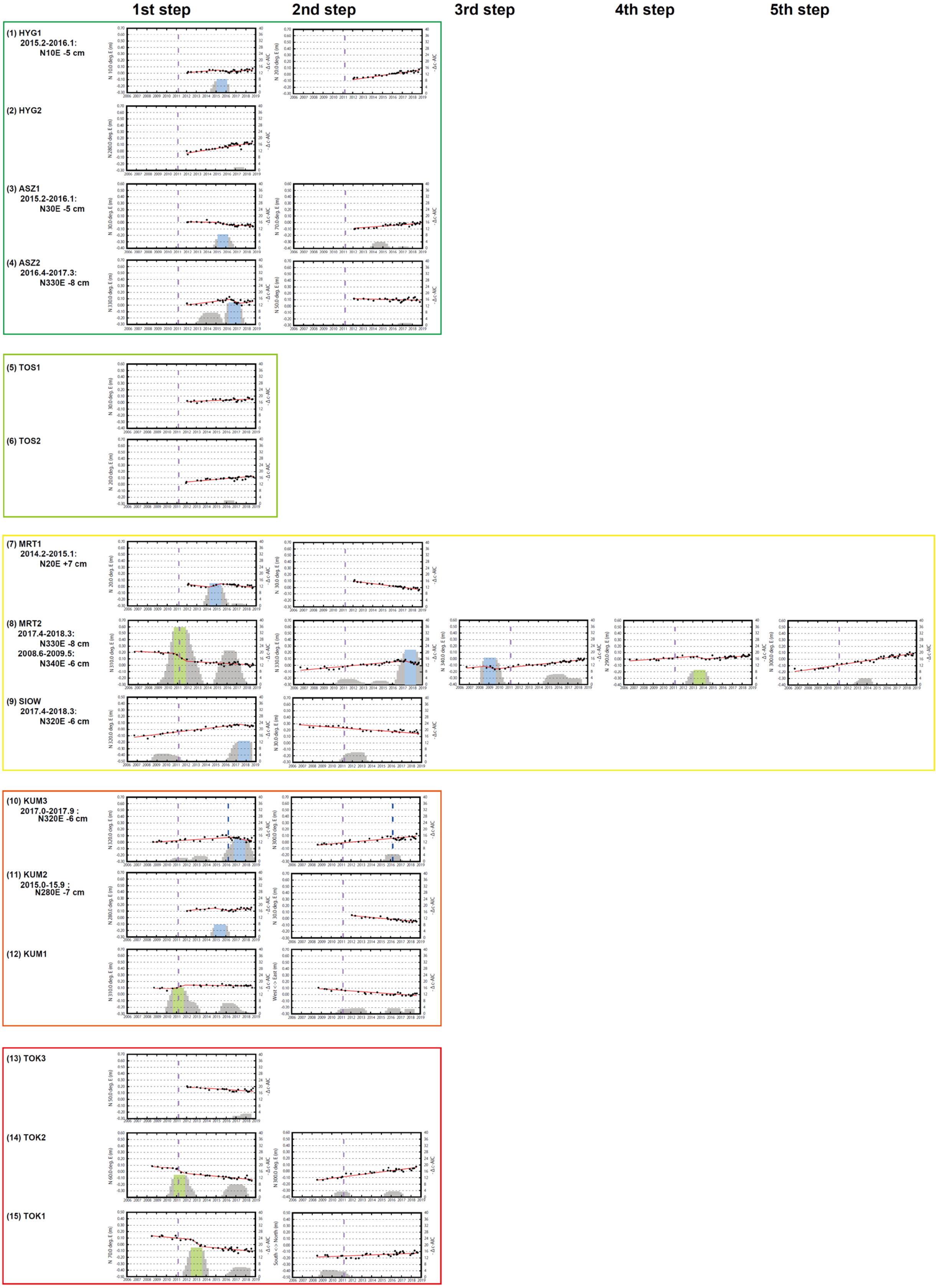

Extended Data Figure 5 | Results of the SSE signal detection process for all the time

series. Each time series was described in the direction with the maximum likelihood solution in the SSE signal detection process. The reference frame is ITRF2005 (ref. 30). The results for each step were obtained in order from the left. Red lines indicate straight and piece-wise lines estimated as the maximum likelihood solutions. Grey histograms are Δc-AIC time series (bin range: one year) in the process every 0.2 years. Light-blue and green bins are Δc-AIC in the cases that were judged as SSE signals and as remaining influences due to the 2011 Tohoku-oki earthquake, respectively. Purple and blue dashed lines indicate the 2011 Tohoku-oki earthquake and the 2016 M_w 5.8 earthquake in the Kumano-nada region, respectively.

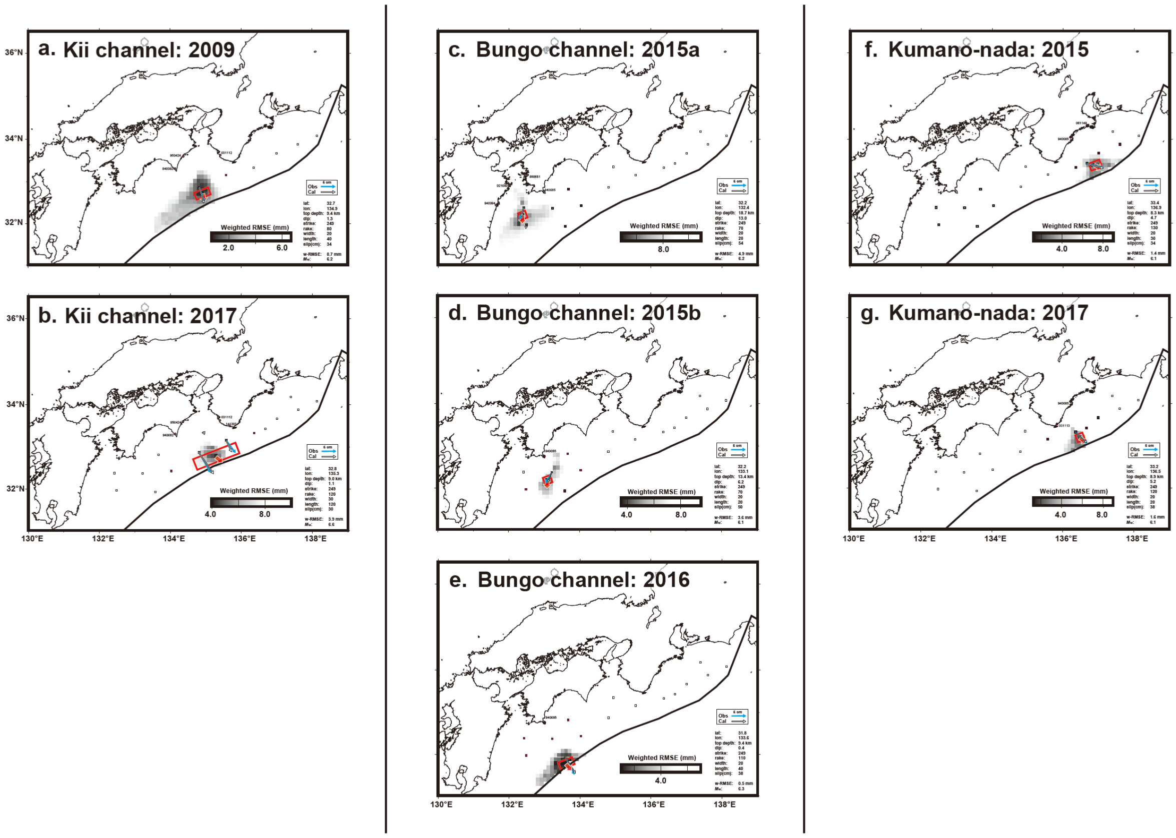

Extended Data Figure 6 | Grid search results for estimating SSE models; a and b, off the Kii channel in 2009 and after 2017, c - e, off the Bungo channel around site (1) and site (3) in 2015 and in 2016 and f and g, around Kumano-nada in 2015 and 2017. Grey regions indicate distributions of SSE model centres with weighted RMSEs calculated in the range between the minimum and 4 mm greater than the minimum. Red rectangles indicate the final obtained rectangular fault models in the results. Blue and white vectors are observed and calculated movements for the sites, respectively. Fault parameters are listed at the right bottom. Pink and light-blue squares and light-blue circles are the seafloor sites moved due to SSEs, unmoved sites and onshore GEONET sites used in the grid search, respectively. GEONET site codes are described beside the sites. Open squares are the seafloor sites that were not used in the grid search.

Supplementary Table legends

Supplementary Table 1 | Time series of seafloor positions. The reference frame is ITRF2005 (ref. 30). The first column shows an observation epoch. Eastward and Northward components (second and third columns) indicate the data corrected the coseismic and postseismic effects due to the Tohoku-oki earthquake. East$_{raw}$ and North$_{raw}$ components (forth and fifth columns) are raw data before March 2014.

(1) HYG1				
Epoch (year)	Eastward (m)	Northward (m)	$East_{raw}$ (m)	$North_{raw}$ (m)
2012.077	0	0	0	0
2012.162	-0.02	0.022	-0.02	0.023
2012.447	-0.018	0.019	-0.017	0.022
2013.044	-0.03	0.022	-0.029	0.028
2013.518	-0.024	0.022	-0.023	0.031
2014.047	-0.059	0.026	-0.057	0.038
2014.318	-0.025	0.054		
2014.66	-0.011	0.05		
2014.942	-0.025	0.041		
2015.411	-0.051	0.04		
2015.696	-0.029	0.041		
2015.94	-0.042	0.035		
2016.044	-0.083	0.04		
2016.219	-0.052	0.018		
2016.334	-0.026	0.005		
2016.485	-0.061	0.032		
2016.608	-0.066	0.039		
2016.775	-0.046	0.057		
2016.877	-0.013	0.046		
2017.047	-0.037	0.026		
2017.104	-0.033	0.006		
2017.208	-0.047	0.027		
2017.466	-0.051	0.03		
2017.575	-0.065	0.064		
2017.874	-0.019	0.044		
2017.94	-0.049	0.054		
2018.129	-0.069	0.073		
2018.192	-0.051	0.031		
2018.351	-0.072	0.068		
2018.605	-0.052	0.042		
2018.696	-0.017	0.074		

(2) HYG2				
Epoch (year)	Eastward (m)	Northward (m)	$East_{raw}$ (m)	$North_{raw}$ (m)
2012.074	0	0	0	0

2012.17	0.062	0.011	0.062	0.011
2012.452	0.025	0.017	0.025	0.019
2013.047	0.03	0.006	0.03	0.011
2013.518	0.016	-0.017	0.017	-0.01
2014.049	0.025	-0.025	0.026	-0.016
2014.321	0.04	0.015		
2014.658	0.036	-0.005		
2014.94	0.041	-0.008		
2015.408	0.032	0.01		
2015.699	0.046	0.001		
2015.948	0.029	0.012		
2016.044	0.033	-0.013		
2016.216	0.058	-0.009		
2016.337	0.026	0.013		
2016.488	0.024	-0.015		
2016.611	0.003	0.004		
2016.775	0.016	0.016		
2016.877	0.028	0.026		
2017.047	0.02	0.004		
2017.107	0.016	0.023		
2017.208	0.032	0.006		
2017.466	0.068	0.011		
2017.575	0.119	-0.019		
2017.874	0.049	0.008		
2017.942	0.025	0		
2018.132	0.029	0.003		
2018.195	0.031	0.006		
2018.345	0.067	0.021		
2018.4	0.063	0.019		
2018.605	0.061	0.008		
2018.699	0.027	0.001		

(3) ASZ1

Epoch (year)	Eastward (m)	Northward (m)	East_{raw} (m)	North_{raw} (m)
2012.077	0	0	0	0
2012.159	-0.002	0.01	-0.002	0.011
2012.455	-0.003	0.021	-0.003	0.025
2013.036	-0.004	0.02	-0.002	0.027

2013.512	-0.01	0.015	-0.008	0.025
2014.044	0.008	0.06	0.011	0.072
2014.315	-0.014	0.02		
2014.945	-0.041	0.035		
2015.195	-0.045	0.085		
2015.405	-0.043	0.056		
2015.663	-0.061	0.05		
2015.701	-0.058	0.062		
2016.058	-0.058	0.037		
2016.334	-0.071	0.043		
2016.49	-0.063	0.037		
2016.614	-0.085	0.062		
2016.773	-0.06	0.038		
2016.877	-0.085	0.022		
2017.047	-0.095	0.038		
2017.107	-0.092	0.025		
2017.208	-0.084	0.049		
2017.575	-0.047	0.008		
2017.871	-0.069	0.021		
2017.942	-0.098	0.073		
2018.129	-0.077	0.075		
2018.195	-0.071	0.042		
2018.351	-0.095	0.023		
2018.397	-0.083	0.076		
2018.608	-0.084	0.032		
2018.69	-0.106	0.056		

(4) ASZ2

Epoch (year)	Eastward (m)	Northward (m)	East$_{raw}$ (m)	North$_{raw}$ (m)
2012.082	0	0	0	0
2012.088	-0.003	0.003	-0.002	0.003
2012.463	-0.002	-0.021	-0.001	-0.019
2013.033	0.012	-0.01	0.013	-0.005
2013.51	0.008	-0.022	0.009	-0.015
2014.041	-0.027	-0.017	-0.025	-0.007
2014.666	-0.018	0.011		
2015.197	-0.043	0.038		
2015.403	-0.045	0.026		

2015.666	-0.079	0.012
2015.704	-0.058	-0.006
2015.951	-0.055	0.026
2016.06	-0.077	0.044
2016.332	-0.083	0.07
2016.501	-0.079	0.025
2016.614	-0.078	0.018
2016.773	-0.105	-0.005
2016.874	-0.069	-0.022
2017.049	-0.044	-0.017
2017.107	-0.02	-0.02
2017.211	-0.046	-0.012
2017.466	-0.076	0.018
2017.578	0.009	-0.028
2017.871	-0.084	-0.011
2018.068	-0.036	-0.001
2018.197	-0.051	0.027
2018.332	-0.041	-0.046
2018.397	-0.075	-0.001
2018.688	-0.116	-0.015

(5) TOS1

Epoch (year)	Eastward (m)	Northward (m)	East$_{raw}$ (m)	North$_{raw}$ (m)
2012.074	0	0	0	0
2012.444	0.002	-0.014	0.003	-0.011
2012.786	-0.028	0.012	-0.026	0.018
2013.068	-0.011	-0.032	-0.008	-0.023
2013.521	-0.022	-0.003	-0.018	0.009
2014.038	-0.018	0.006	-0.013	0.021
2014.668	-0.018	0.029		
2014.951	-0.04	0.032		
2015.414	-0.046	0.038		
2015.707	-0.071	0.014		
2015.937	-0.056	0.022		
2016.055	-0.076	0.029		
2016.321	-0.068	0.024		
2016.49	-0.083	0.033		
2016.778	-0.08	0.056		

2016.879	-0.112	0.05
2017.049	-0.094	0.001
2017.104	-0.087	0.002
2017.205	-0.109	0.027
2017.581	-0.071	0.012
2017.877	-0.087	0.032
2017.945	-0.103	0.031
2018.192	-0.1	0.072
2018.329	-0.096	0.062
2018.608	-0.127	0.047
2018.69	-0.09	0.043

(6) TOS2

Epoch (year)	Eastward (m)	Northward (m)	East$_{raw}$ (m)	North$_{raw}$ (m)
2011.904	0	0	0	0
2011.951	-0.033	0.008	-0.033	0.008
2013.055	-0.058	0.022	-0.056	0.031
2013.419	-0.079	0.009	-0.076	0.021
2013.899	-0.083	0.036	-0.079	0.05
2014.06	-0.046	0.056	-0.043	0.072
2014.312	-0.061	0.04		
2014.948	-0.071	0.035		
2015.4	-0.071	0.047		
2015.668	-0.11	0.032		
2015.704	-0.098	0.043		
2016.222	-0.11	0.05		
2016.329	-0.106	0.043		
2016.479	-0.108	0.036		
2016.616	-0.113	0.041		
2016.773	-0.052	0.014		
2016.874	-0.129	0.033		
2017.049	-0.124	0.013		
2017.118	-0.128	0.043		
2017.211	-0.134	0.05		
2017.578	-0.096	0.017		
2017.868	-0.132	0.014		
2017.932	-0.149	0.055		
2018.068	-0.127	0.062		

2018.197	-0.125	0.057
2018.395	-0.134	0.063
2018.688	-0.146	0.043

(7) MRT1

Epoch (year)	Eastward (m)	Northward (m)	East$_{raw}$ (m)	North$_{raw}$ (m)
2012.09	0	0	0	0
2012.156	0.003	0.018	0.003	0.02
2012.438	-0.023	-0.005	-0.021	0
2012.775	-0.019	-0.011	-0.016	-0.003
2013.425	-0.042	-0.029	-0.036	-0.014
2013.896	-0.061	-0.03	-0.053	-0.01
2014.674	-0.034	-0.02		
2014.967	-0.05	-0.003		
2015.674	-0.071	0.013		
2016.063	-0.084	0.017		
2016.318	-0.083	0.013		
2016.477	-0.069	0.002		
2016.627	-0.066	0.003		
2016.778	-0.105	0.021		
2016.879	-0.084	0.003		
2017.052	-0.103	-0.019		
2017.101	-0.101	-0.01		
2017.197	-0.089	0.003		
2017.581	-0.083	-0.032		
2017.877	-0.09	-0.034		
2018.126	-0.097	-0.001		
2018.329	-0.107	-0.006		
2018.515	-0.102	-0.006		
2018.611	-0.153	-0.034		
2018.685	-0.126	-0.026		

(8) MRT2

Epoch (year)	Eastward (m)	Northward (m)	East$_{raw}$ (m)	North$_{raw}$ (m)
2006.668	0	0	0	0
2007.351	0.025	-0.01	0.024	-0.009
2008.71	0.014	-0.011	0.013	-0.011

2009.11	-0.003	0.012	-0.004	0.012
2009.332	-0.006	-0.017	-0.006	-0.017
2009.556	0.002	-0.042	0.001	-0.041
2010.049	0.021	-0.029	0.02	-0.029
2010.603	-0.006	-0.032	-0.007	-0.031
2010.956	-0.044	-0.019	-0.045	-0.018
2011.441	-0.084	-0.06	-0.04	-0.043
2011.951	-0.102	-0.064	-0.056	-0.039
2012.784	-0.142	-0.079	-0.093	-0.046
2013.058	-0.147	-0.078	-0.099	-0.042
2013.422	-0.115	-0.077	-0.065	-0.038
2013.893	-0.167	-0.088	-0.116	-0.046
2014.304	-0.181	-0.089		
2014.671	-0.173	-0.105		
2014.953	-0.184	-0.054		
2015.178	-0.199	-0.082		
2015.425	-0.215	-0.07		
2015.671	-0.186	-0.07		
2015.715	-0.235	-0.09		
2016.225	-0.197	-0.05		
2016.318	-0.226	-0.069		
2016.504	-0.237	-0.054		
2016.619	-0.225	-0.042		
2016.77	-0.188	-0.043		
2016.871	-0.194	-0.048		
2017.121	-0.18	-0.049		
2017.211	-0.218	-0.06		
2017.321	-0.245	-0.051		
2017.877	-0.21	-0.066		
2017.932	-0.197	-0.076		
2018.071	-0.203	-0.077		
2018.2	-0.2	-0.102		
2018.329	-0.239	-0.097		
2018.512	-0.194	-0.11		
2018.611	-0.177	-0.088		
2018.685	-0.21	-0.086		

(9) SIOW

Epoch (year)	Eastward (m)	Northward (m)	$East_{raw}$ (m)	$North_{raw}$ (m)
2006.693	0	0	0	0
2007.647	-0.034	-0.03	-0.034	-0.03
2008.038	0.006	-0.059	0.006	-0.059
2008.71	-0.006	-0.028	-0.006	-0.029
2009.323	-0.039	-0.009	-0.039	-0.009
2009.553	-0.05	-0.005	-0.05	-0.006
2010.047	-0.061	0.006	-0.061	0.005
2010.603	-0.061	0.01	-0.061	0.01
2011.063	-0.107	0.008	-0.107	0.008
2011.441	-0.112	0.01	-0.062	0.03
2011.948	-0.119	0.003	-0.065	0.032
2012.778	-0.122	-0.009	-0.065	0.03
2013.063	-0.174	-0.026	-0.116	0.017
2013.427	-0.15	-0.023	-0.091	0.023
2013.89	-0.218	-0.003	-0.157	0.048
2014.682	-0.185	-0.006		
2014.973	-0.212	0.005		
2015.655	-0.208	0.022		
2016.071	-0.228	-0.01		
2016.315	-0.227	0.014		
2016.474	-0.22	-0.005		
2016.781	-0.256	0.003		
2016.882	-0.216	0.032		
2017.058	-0.237	0.024		
2017.214	-0.222	0.023		
2017.879	-0.242	0.007		
2018.123	-0.244	-0.002		
2018.326	-0.228	-0.013		
2018.515	-0.226	0.015		
2018.614	-0.248	-0.014		
2018.682	-0.264	-0.028		

(10) KUM3

Epoch (year)	Eastward (m)	Northward (m)	$East_{raw}$ (m)	$North_{raw}$ (m)
2008.707	0	0	0	0
2009.112	-0.009	-0.007	-0.009	-0.008

2009.334	-0.018	0.011	-0.018	0.01
2009.551	-0.006	0.002	-0.006	0.002
2010.06	-0.022	-0.042	-0.022	-0.043
2010.6	-0.02	-0.012	-0.02	-0.013
2011.058	-0.021	-0.012	-0.021	-0.012
2011.438	-0.071	-0.017	-0.015	0.005
2011.899	-0.075	-0.016	-0.015	0.015
2011.945	-0.093	-0.017	-0.033	0.015
2012.795	-0.069	-0.036	-0.006	0.008
2013.43	-0.07	-0.042	-0.004	0.009
2013.888	-0.097	0.015	-0.029	0.07
2014.685	-0.087	-0.031		
2015.175	-0.122	0.005		
2015.677	-0.13	0.027		
2016.038	-0.122	0.031		
2016.312	-0.103	0.012		
2016.507	-0.11	-0.026		
2016.633	-0.123	-0.069		
2016.781	-0.141	-0.031		
2016.882	-0.058	0.035		
2017.033	-0.087	0.004		
2017.121	-0.111	-0.009		
2017.214	-0.114	-0.02		
2017.318	-0.133	-0.016		
2017.468	-0.072	-0.002		
2017.879	-0.123	-0.028		
2018.058	-0.06	-0.057		
2018.189	-0.088	-0.015		
2018.326	-0.087	-0.043		
2018.392	-0.098	-0.077		
2018.518	-0.057	-0.033		
2018.616	-0.154	-0.046		

(11) KUM2

Epoch (year)	Eastward (m)	Northward (m)	East$_{raw}$ (m)	North$_{raw}$ (m)
2012.093	0	0	0	0
2012.427	-0.009	-0.02	-0.008	-0.015
2013.074	-0.043	-0.009	-0.039	0.005

2013.433	-0.027	-0.028	-0.021	-0.01
2013.885	-0.033	-0.045	-0.026	-0.023
2014.299	-0.051	-0.032		
2014.975	-0.057	-0.007		
2015.652	-0.012	-0.024		
2015.723	-0.037	-0.047		
2016.036	-0.026	-0.028		
2016.348	-0.006	-0.044		
2016.507	-0.017	-0.028		
2016.633	-0.032	-0.039		
2016.784	0	-0.052		
2017.03	-0.015	-0.057		
2017.214	-0.048	-0.048		
2017.468	-0.035	-0.031		
2017.584	-0.062	-0.02		
2017.882	-0.057	-0.049		
2018.058	-0.024	-0.041		
2018.192	-0.058	-0.049		
2018.323	-0.04	-0.034		
2018.521	-0.03	-0.049		
2018.616	-0.062	-0.021		

(12) KUM1

Epoch (year)	Eastward (m)	Northward (m)	East$_{raw}$ (m)	North$_{raw}$ (m)
2008.729	0	0	0	0
2009.337	0	-0.02	-0.001	-0.02
2009.551	-0.02	-0.024	-0.021	-0.024
2010.041	0.021	-0.053	0.021	-0.053
2010.597	0.001	-0.018	0.001	-0.018
2011.055	-0.022	-0.034	-0.022	-0.034
2011.438	-0.056	-0.027	0.011	0
2012.773	-0.074	-0.027	0.003	0.025
2013.408	-0.086	-0.045	-0.006	0.015
2013.507	-0.081	-0.063	0	-0.002
2014.066	-0.103	-0.052	-0.019	0.016
2014.69	-0.07	-0.036		
2015.2	-0.099	-0.074		
2015.647	-0.136	-0.069		

2016.036	-0.113	-0.076
2016.351	-0.118	-0.076
2016.51	-0.104	-0.066
2016.784	-0.039	-0.036
2017.03	-0.082	-0.046
2017.216	-0.113	-0.085
2017.584	-0.113	-0.086
2017.882	-0.1	-0.072
2018.074	-0.128	-0.091
2018.121	-0.109	-0.081
2018.203	-0.108	-0.086
2018.323	-0.092	-0.064
2018.521	-0.092	-0.053
2018.701	-0.044	-0.053

(13) TOK3

Epoch (year)	Eastward (m)	Northward (m)	East$_{raw}$ (m)	North$_{raw}$ (m)
2012.096	0	0	0	0
2012.153	-0.01	-0.015	-0.01	-0.014
2012.422	-0.022	0.004	-0.019	0.012
2013.077	0.009	-0.032	0.017	-0.013
2013.436	-0.02	-0.02	-0.009	0.005
2013.91	-0.025	-0.026	-0.009	0.006
2014.293	-0.055	-0.028		
2015.17	-0.056	-0.015		
2015.644	-0.032	-0.029		
2015.825	-0.044	-0.024		
2016.033	-0.05	-0.015		
2016.353	-0.088	-0.004		
2016.636	-0.073	-0.045		
2016.786	-0.079	-0.04		
2017.03	-0.04	-0.081		
2017.216	-0.056	-0.018		
2017.885	-0.042	-0.024		
2018.044	-0.06	-0.038		
2018.181	-0.083	-0.037		
2018.321	-0.072	-0.045		
2018.521	-0.052	-0.029		

2018.704	-0.056	0.017		

(14) TOK2

Epoch (year)	Eastward (m)	Northward (m)	East_{raw} (m)	North_{raw} (m)
2008.529	0	0	0	0
2009.104	-0.003	-0.014	-0.003	-0.014
2009.548	-0.03	-0.019	-0.031	-0.019
2010.063	-0.04	0.011	-0.04	0.011
2010.595	-0.032	-0.01	-0.032	-0.01
2010.964	-0.047	-0.01	-0.047	-0.01
2011.066	-0.053	0.014	-0.053	0.014
2011.436	-0.119	0.006	-0.045	0.037
2011.942	-0.118	-0.002	-0.036	0.043
2012.77	-0.13	-0.033	-0.044	0.026
2013.405	-0.131	-0.023	-0.041	0.045
2013.882	-0.162	-0.016	-0.069	0.057
2014.068	-0.149	-0.029	-0.055	0.047
2014.296	-0.157	-0.027		
2015.203	-0.182	0		
2015.641	-0.18	-0.01		
2015.726	-0.226	0.001		
2015.932	-0.18	-0.019		
2016.227	-0.181	-0.039		
2016.378	-0.188	-0.046		
2016.512	-0.206	-0.028		
2016.501	-0.214	-0.012		
2016.784	-0.208	-0.016		
2017.06	-0.206	-0.048		
2017.216	-0.157	-0.04		
2017.885	-0.186	-0.009		
2018.044	-0.152	0.007		
2018.192	-0.207	-0.024		
2018.321	-0.212	-0.026		
2018.523	-0.255	-0.009		

(15) TOK1

Epoch (year)	Eastward (m)	Northward (m)	East_{raw} (m)	North_{raw} (m)

2008.54	0	0	0	0
2009.34	-0.014	0.009	-0.014	0.009
2009.545	0.009	0.009	0.009	0.009
2009.627	0.007	-0.014	0.007	-0.014
2010.595	-0.039	-0.032	-0.04	-0.032
2010.948	0.008	-0.003	0.008	-0.004
2011.068	-0.028	-0.002	-0.028	-0.002
2011.436	-0.056	-0.029	0.027	0.005
2011.942	-0.045	-0.034	0.048	0.014
2012.419	-0.04	-0.044	0.056	0.013
2012.71	-0.056	-0.038	0.042	0.024
2013.085	-0.102	-0.027	-0.002	0.041
2013.403	-0.148	-0.038	-0.046	0.035
2013.501	-0.132	-0.03	-0.03	0.044
2013.879	-0.15	-0.038	-0.045	0.041
2014.693	-0.176	-0.067		
2015.205	-0.184	-0.034		
2015.641	-0.201	-0.043		
2015.726	-0.221	-0.052		
2015.923	-0.16	-0.069		
2016.23	-0.214	-0.044		
2016.356	-0.208	0.011		
2016.515	-0.176	-0.016		
2016.504	-0.195	-0.044		
2016.597	-0.218	-0.04		
2016.786	-0.245	-0.019		
2016.885	-0.239	-0.005		
2017.123	-0.193	0.007		
2017.219	-0.275	-0.017		
2017.888	-0.209	-0.053		
2018.041	-0.203	-0.031		
2018.195	-0.237	-0.026		
2018.318	-0.261	0.017		
2018.523	-0.207	-0.006		
2018.619	-0.247	-0.016		